Precision 3D-Printed Cell Scaffolds Mimicking Native Tissue Composition and Mechanics

Amelie Erben, Marcel Hörning, Bastian Hartmann, Tanja Becke, Stephan A. Eisler, Alexander Southan, Séverine Cranz, Oliver Hayden, Nikolaus Kneidinger, Melanie Königshoff, Michael Lindner, Günter E. M. Tovar, Gerald Burgstaller, Hauke Clausen-Schaumann, Stefanie Sudhop,* and Michael Heymann*

Cellular dynamics are modeled by the 3D architecture and mechanics of the extracellular matrix (ECM) and vice versa. These bidirectional cell-ECM interactions are the basis for all vital tissues, many of which have been investigated in 2D environments over the last decades. Experimental approaches to mimic in vivo cell niches in 3D with the highest biological conformity and resolution can enable new insights into these cell-ECM interactions including proliferation, differentiation, migration, and invasion assays. Here, two-photon stereolithography is adopted to print up to mm-sized high-precision 3D cell scaffolds at micrometer resolution with defined mechanical properties from protein-based resins, such as bovine serum albumin or gelatin methacryloyl. By modifying the manufacturing process including two-pass printing or post-print crosslinking, high precision scaffolds with varying Young's moduli ranging from 7-300 kPa are printed and quantified through atomic force microscopy. The impact of varying scaffold topographies on the dynamics of colonizing cells is observed using mouse myoblast cells and a 3D-lung microtissue replica colonized with primary human lung fibroblast. This approach will allow for a systematic investigation of single-cell and tissue dynamics in response to defined mechanical and bio-molecular cues and is ultimately scalable to full organs.

1. Introduction

Understanding the interactions between cells and the extracellular matrix (ECM) of respective tissue has been a decades-long, still ongoing effort by a broad interdisciplinary community. In particular, new methodological advances ranging from high-resolution imaging[1,2] over proteomics and transcriptomics[3,4] to computational modeling[5] have expanded our understanding of the molecular composition and architecture of the ECM. Micro-scale ECM properties have been identified as being pivotal in controlling and guiding cellular growth, migration, and differentiation, to ultimately define tissue architecture.[6,7] Besides mechanical and biochemical signals, the geometry of the ECM is essential to direct cellular response.[8–11] While this is the case for every organ type, there are specific tissues that emphasize the importance of highly resolved structures within the human body. These include for example the organization of individual

A. Erben, B. Hartmann, Dr. T. Becke, Prof. H. Clausen-Schaumann, Dr. S. Sudhop
Center for Applied Tissue Engineering and Regenerative Medicine
Munich University of Applied Sciences
Lothstr. 34, Munich 80533, Germany
E-mail: stefanie.sudhop@hm.edu

A. Erben, Prof. O. Hayden
Heinz-Nixdorf-Chair of Biomedical Electronics, TranslaTUM, Campus Klinikum rechts der Isar
Technical University of Munich
Einsteinstraße 25, Munich 81675, Germany

A. Erben, B. Hartmann, Dr. T. Becke, Prof. H. Clausen-Schaumann, Dr. S. Sudhop, Prof. M. Heymann
Center for NanoScience (CeNS)
Ludwig-Maximilians-University
Geschwister-Scholl Platz 1, Munich 80539, Germany
E-mail: michael.heymann@bio.uni-stuttgart.de

Dr. M. Hörning, Prof. M. Heymann
Institute of Biomaterials and Biomolecular Systems
University of Stuttgart
Pfaffenwaldring 57, Stuttgart 70569, Germany

Dr. S. A. Eisler
Stuttgart Research Center Systems Biology
University of Stuttgart
Nobelstr. 15, Stuttgart 70569, Germany

Dr. A. Southan, Prof. G. E. M. Tovar
Institute of Interfacial Process Engineering and Plasma Technology IGVP
University of Stuttgart
Nobelstr. 12, Stuttgart 70569, Germany

S. Cranz, Dr. N. Kneidinger, Prof. M. Königshoff, Dr. M. Lindner, Dr. G. Burgstaller
Institute of Lung Biology and Disease and Comprehensive Pneumology Center with the CPC-M bioArchive, Helmholtz Zentrum München
Member of the German Center for Lung Research (DZL)
Max-Lebsche-Platz 31, Munich 81377, Germany

**ADVANCED
SCIENCE NEWS**

www.advancedsciencenews.com

**ADVANCED
HEALTHCARE
MATERIALS**

www.advhealthmat.de

cell layers within retinal tissue,[12] the basal membrane separating maternal from fetal blood in the placenta[13] or the alveoli located within the lung at the ends of the branched respiratory tract. In the latter example, the thin air-blood membrane separating perfused capillaries from oxygen-filled air sacs enables a sufficient gas exchange which ensures adequate oxygenation of the blood.[14]

The aim to use high-resolution insights of cell and tissue architectures is currently prompting a resolution revolution in the field of biofabrication. This quest, to ultimately recreate the in vivo matrix in all its detail, continues to inspire new fabrication method developments.[15–17] Initially limited to 2D micro-patterning, such as elastomere stamps,[18,19] spotted DNA microarrays,[20] or polyacrylamide gels,[21] additive manufacturing increasingly expanded the capacity to engineer cell and tissue environments in vitro.[22] In particular, one-photon stereolithography and volumetric bioprinting achieved fast fabrication of clinically relevantly sized tissue constructs of protein-based resins at two-digit µm scale resolution.[23,24] To ultimately recapitulate in vivo 3D tissue ultrastructure, further resolution improvements to bellow the single cell size are required.[22] Excitation of two photons in spatial and temporal proximity can increase resolution in additive manufacturing, as was initially explored in microscopy.[25] Two-photon stereolithography (TPS) of complex sub-micrometer resolved geometries were shown to guide cell adhesion[26] and cardiomyocyte differentiation,[27] when synthetic resins were functionalized with appropriate cell-mediating biomolecules. Extending TPS to accurately structure protein-based resins that attain essential in vivo biochemical and biophysical properties offers tantalizing avenues for tissue engineering, cell, and developmental biology.

However, the experimental realization of TPS using protein-based resins poses several challenges. First, in voxel-based additive manufacturing the spatial resolution and print time are inversely linked to each other and are restricted by the 3D voxel size, making it difficult to scale-up printing results.[23] Uncon-

trolled water evaporation can quickly, within minutes, degrade protein-based resin quality during the printing process, limiting available printing times to under an hour. Alternatively, print volumes are contained in microfluidic perfusion chambers.[13] Furthermore, the accurate mechanical characterization of micronsized protein-based scaffolds remains challenging and the absence of universal analysis standards limits the comparability of results between labs.

Beginning with bovine serum albumin (BSA) and rose bengal (RB), various photoactivatable protein-based resins have been introduced to TPS[28] to print scaffolds for subsequent colonization with cells (Table S1, Supporting Information).[29–31] Other commonly used fluorescent photo-initiators, such as methylene blue, eosin Y or rhodamine B have also been used in combination with BSA.[32,33] While fluorescent cell scaffolds might be beneficial for specific applications, the intensity of residual photoinitiators such as RB within printed structures evokes high fluorescent background signals in the range from green to red often exceeding the signal of fluorescently labeled cells within scaffolds.[29,34] Furthermore, BSA is not native to the ECM and is therefore not ideal for cell cultivation. Hence, several groups have explored ECM proteins for their compatibility to a broad range of bioprinting methods,[35,36] including gelatin methacryloyl derivatives for TPS.[13,37–39] Despite beneficial cell adhesion properties of commercially available gelatin methacryloyl (GelMa), the gelation of GelMa at room temperature makes it difficult to achieve structures higher than the available objective working distance without a heated printing chamber. Hence, Engelhardt et al. explored gelatin methacrylamide (Gel-MAAm) with a high degree of methacrylation at amino and hydroxyl groups, preventing gelation at room temperature.[9] A similar approach was pursued by Van Hoorick et al. by introducing Gel-MOD-AEMA with modifications of amino and carboxyl groups for TPS.[13,40] Both gelatin derivatives are characterized by their good TPS processivity and resulting shape fidelity.

Bioprinting seeks to replicate the broad range of stiffnesses exhibited in native tissues, as for example the lung (0.2–2 kPa) and cartilage (500–1700 kPa).[41,42] Various biofabrication techniques have achieved these mechanical properties using gelatin and its derivatives.[35,43] To realize an equally broad spectrum of mechanical properties in TPS printed ECM derived scaffolds would hence be highly desirable. This requires accurate mechanical analysis of small TPS samples. The Young's modulus (YM) of micro- to nanoscale structures has been estimated by nanoindentation,[44] laser Doppler vibrometry[45] or indentation-type atomic force microscopy (IT-AFM).[33,46] AFM is a versatile approach to measure both the topography as well as the mechanical properties of materials and is applied throughout the materials and life sciences.[47–50] It is particularly valuable for biological samples, as measurements can be conducted in a physiological environment. For the mechanical characterization of microscopic hydrogel probes, IT-AFM has emerged as the method of choice and several groups reported specific values for the YM for TPS protein scaffolds,[33,51] including gelatin based resin for 2–7 kPa scaffolds.[52] AFM analysis provides nanometer spatial resolution and senses pN forces. Thus, AFM is ideally suited to determine the mechanical properties of TPS printed scaffolds to ultimately provide each mammalian cell type, including primary cells, with the optimal ECM environment.

S. Cranz, Prof. M. Königshoff
Research Unit Lung Repair and Regeneration
Helmholtz Zentrum München
Max-Lebsche-Platz 31, Munich 81377, Germany

Dr. N. Kneidinger
Department of Internal Medicine V
Ludwig-Maximillians-University Munich
Marchioninistr. 15, Munich 81377, Germany

Prof. M. Königshoff
University of Colorado
Department of Pulmonary Sciences and Critical Care Medicine
13001 E. 17th Pl., Aurora, CO 80045, USA

Dr. M. Lindner
University Department of Visceral and Thoracic Surgery Salzburg
Paracelsus Medical University
Müllner Hauptstraße 48, Salzburg A-5020, Austria

Dr. G. Burgstaller
Institute of Lung Biology and Disease (ILBD)
Helmholtz Zentrum München
Max-Lebsche-Platz 31, Munich 81377, Germany

Prof. M. Heymann
Department of Cellular and Molecular Biophysics
MPI of Biochemistry Martinsried
Am Klopferspitz 18, Planegg 82152, Germany

**ADVANCED
SCIENCE NEWS**

www.advancedsciencenews.com

**ADVANCED
HEALTHCARE
MATERIALS**

www.advhealthmat.de

Here, we introduce a custom dip-in setup for a TPS protein-based resin workflow to achieve up-scaled construct sizes while maintaining high-resolution features. The setup allows for a continuous working distance adjustment and simultaneously provides humidity to the printing environment. As a result, the printing time window with defined resin composition is significantly extended. Using our TPS protein-based resin containing GM10, as a gelatin derivative with a high degree of methacrylation[53] and the photo-initiator LAP (lithium phenyl-2,4,6-trimethylbenzoylphosphinate), we achieve robust room temperature prints with low auto fluorescence and YM ranging from 7 to 300 kPa. AFM analysis of these scaffolds reveals the dependence of the Young's modulus on different manufacturing aspects, such as objective magnification, laser power, and post-crosslinking. By colonizing resulting 3D printed high-precision cell scaffolds with human mesenchymal stem cells (hMSCs), mouse tendon stem/progenitor cells (mTSPCs), murine NIH3T3 fibroblast wildtype cells (NIH3T3 WT), human umbilical vein endothelial cells (HUVECs), and primary human lung fibroblasts (phLFs) we demonstrate good cell compatibility and universal applicability of our constructs. Finally, our high-precision scaffolds colonized with C2C12 mouse myoblast cells or phLFs serve as an in vitro model to demonstrate the utility of our constructs to simultaneously investigate the effects of 3D spatial confinement and mechanical properties on cell alignment.

2. Results and Discussion

2.1. Dip-In TPS for Precision Large Scale 3D Bioprinting

To fabricate highly resolved structures mimicking native tissue, we used confocal microscopy data to generate a 3D printing template for TPS. As a proof of principle, we chose a decellularized mouse lung and digitized a $300 \times 300 \times 300$ μm³ section representing the lung's parenchymal alveolar tissue.[41] Available 3D confocal microscopy data in VRML2 file format was converted and exported to printable STL format using the open-source MeshLab rendering software (**Figure 1**A).[54] In a bottom-up TPS configuration, in which the laser was focused through an inert immersion oil to polymerize resin on the distal substrate interface, the maximal structure height which we could achieve for protein-based resins was of order 14 μm (Figure 1B). This was well below the available mechanical clearance of the used objectives which is about 200 μm above the microscope slide surface, indicating extensive scattering losses across the various interfaces, as well as the previously printed scaffold layers themselves. To increase achievable print heights, we converted the set-up to allow for dip-in printing of protein-based resins (Figure 1C). In dip-in mode, the resin simultaneously acts as immersion medium.[25] By applying 15 μL of protein-based resin directly to the 40× objective lens (numerical aperture (NA) 1.2), we were able to fabricate a $222 \times 222 \times 104$ μm³ alveolar section in about 37 min printing time. However, due to the prolonged printing time a continued solvent evaporation from the hydrogel resin resulted in resin gelation and laser-induced bubble formation that we attribute to local heating due to the laser-induced exothermic cross-linking reaction. As even subtle variations in resin composition severely altered resulting scaffold mechanics, we set out to prevent evaporative loss throughout the print job.

In bottom-up print mode, evaporation can easily be prevented by using a resin cover, such as a silicon lid or a microfluidic device, that contains the resin drop.[29] For dip-in mode, we 3D printed a flexible water reservoir with conventional stereolithography that seals around the objective and the 35 mm cell culture dish. The design allows for objective translations while also maintaining humidity around the resin drop during printing. As a result, we achieved intact large-scale prints (Figure 1C). We thus continued to use this custom dip-in configuration for all subsequent fabrications. To further reduce printing times, we switched from a 40× objective to a 25× objective (NA 0.8). This allowed adjustment of the distance between individual layers (slicing) from 0.3 to 1 μm and x/y spacing between voxels from 0.2 to 0.5 μm, reducing the print time for the $222 \times 222 \times 104$ μm³ alveolar section to 6 min (Table S2, Supporting Information). Taken together, the dip-in approach in combination with our humidified printing chamber allowed for 3D printing of scaffolds exceeding millimeter sizes while preserving low micron resolution when printing directly into standard cell culture petri dishes.

2.2. Optimized Biopolymer Resin for Non-Fluorescent Biocompatible 3D Scaffolds

The ideal resin for TPS conveys the highest possible chemical and biomechanical similarity with native ECM, without introducing undesired fluorescent background from residual photo-initiators. Due to the widespread use of BSA-RB and gelatin methacryloyl for TPS and related bioprinting studies in the past,[30,37,46,55] we benchmarked our results against both of these systems using our dip-in setup (Table S1, Supporting Information). A mesh structure with 5 μm holes underpinned by several posts was designed with the CAD software SolidWorks (**Figure 2**A1) and then 3D printed from BSA-RB resin using a 25× objective (Figure 2A2–A4, green). BSA resin is an easy-to-use composition for TPS applications producing highly resolved, biocompatible scaffolds.[56] However, it is not a natural component of the ECM's matrisome and thus only poorly supports cellular attachment. Therefore, scaffolds were coated with the ECM glycoprotein fibronectin,[57] which provided molecular attachment sites for cells most likely mediated by integrin receptors. Subsequently, the coated scaffolds were colonized with hMSCs. In time lapse microscopy we observed a successful attachment of hMSCs to scaffolds as well as initial spreading, followed by active cellular migration (Movie S1, Supporting Information). After 2.5 days of incubation, hMSCs were fixed and the actin cytoskeleton was stained with ATTO 594 phalloidin (Figure 2A2–A4, red). Top, side, and bottom view confocal 3D images demonstrated that hMSCs were located on top of the scaffold's mesh structure as well as on the glass substrate in between the posts. This implies that the hMSCs were actively migrating through the 5 μm holes and arranged themselves within the spatial architecture of 3D printed scaffolds, consistent with previous reports using, for example, foreskin fibroblasts (Table S1, Supporting Information).[37]

To further increase the biochemical similarity of the scaffolds with respect to the natural ECM composition, commercially available GelMa has already been used in TPS. GelMa has cell adhesive properties comprising arginine-glycine-aspartic acid tripeptides,[21,35,43] providing integrin-based cell attachment
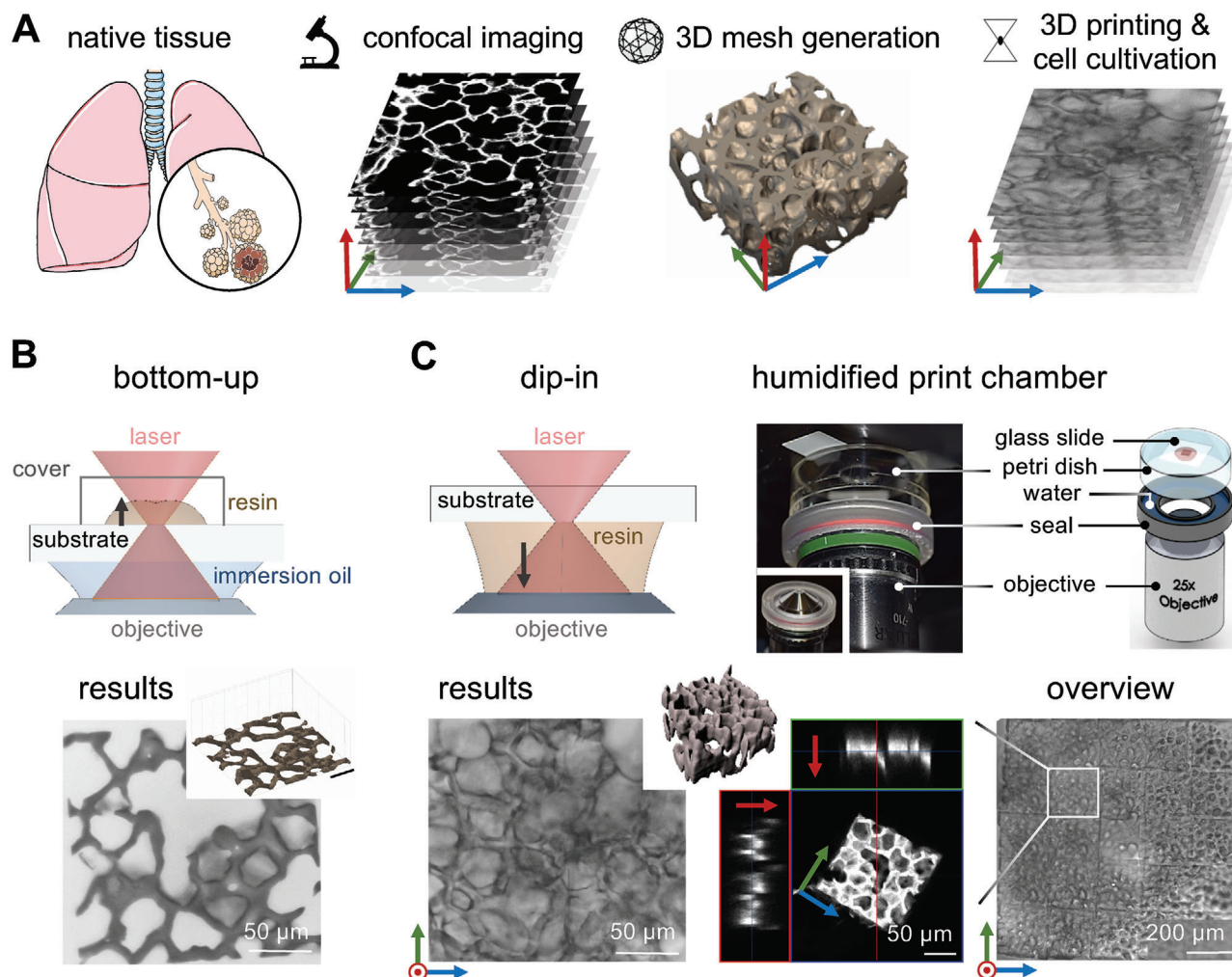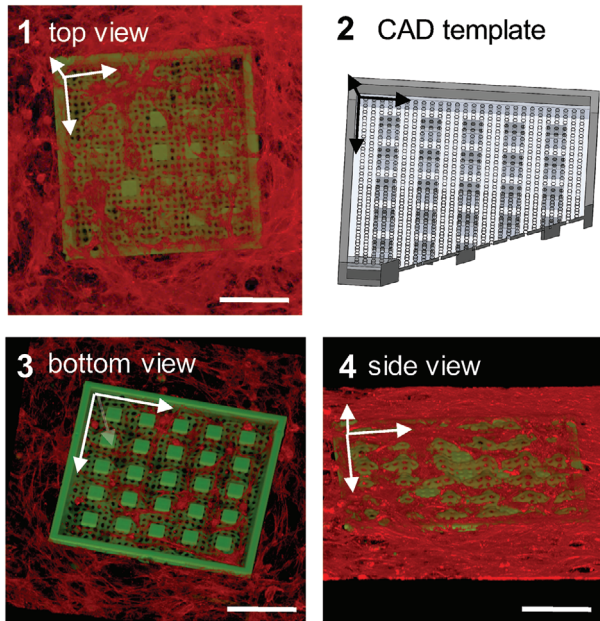
Figure 1. Workflow and dip-in setup for biological resins. A) Every organ has a highly specific and complex microstructure, such as the lung with alveoli at the distal ends of the respiratory tree. High-resolution 3D imaging of these microstructures, for example, by confocal or light sheet microscopy can be utilized to generate 3D print templates. Through selective exposure, two-photon stereolithography can generate a geometric tissue analogue in vitro by polymerizing photo-activatable, protein-based resin in a layer-by-layer fashion. B) Two-photon 3D printing of aqueous protein-based resins is predominantly done in bottom-up mode, in which the laser is focused through an immersion oil to polymerize voxels on the opposite side of the cover slip substrate. In this setup, the evaporation of resin can easily be prevented through a water-proof containment sealing the resin drop with the glass slide. However, this printing mode is limited in height by the working distance of the used objective and by light-scattering at already processed sample layers. C) In dip-in mode, the resin simultaneously acts as immersion medium, allowing for a constant adjustment of the working distance to obtain structures of in principle any height. In the case of hydrogel resins, however, the printing process is quickly compromised by solvent evaporation, imposing a temporal limit on permissive print volumes. By means of a dedicated objective seal, resin evaporation was prevented for hours allowing long-term dip-in mode printing to obtain printed structures in the range of mm into standard 35 mm cell culture petri dishes (Table S2, Supporting Information, $n > 25$).
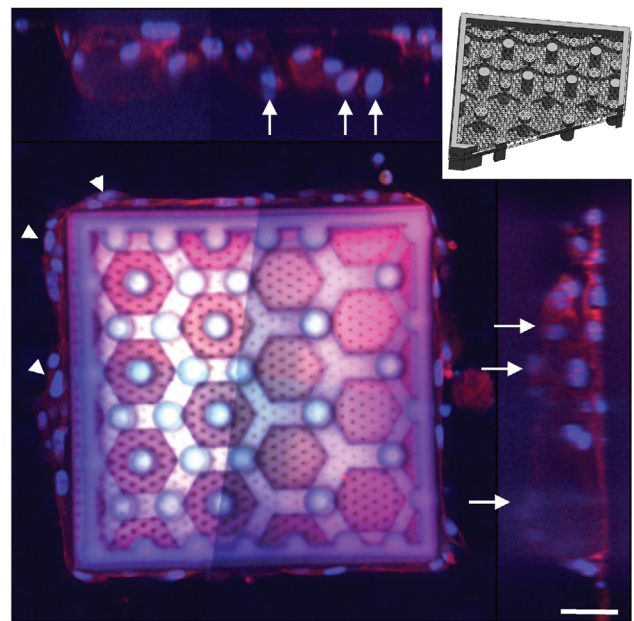
sites in the resin itself. In our experiments, resin compositions containing 25 wt% GelMa and RB in the ratio 9:1 were only processable at room temperature in a gelled state. As gelation prevented the objective from dipping in, we explored printing into about 200–300 µm thin GelMa gel layers, whose height was well below the objective working distance. With a diluted photo-initiator pre-mix as immersion fluid, the objective travel was thus not constrained by gelled GelMa. However, printing large structures proved difficult following this approach, as the deposited gelatin continuously dissolved in the aqueous immersion medium during printing, consequently diluting the resin composition and limiting the total printing time. In an alterna-

tive approach, we therefore supplemented the BSA pre-mix solution with 25 wt% GelMa pre-mix solution in the ratio 4:1 before adding RB, resulting in final concentrations of 28.8 wt% BSA and 4.5 wt% GelMa. This was the highest GelMa concentration that could still be processed at room temperature. phLFs adhered to all scaffolds fabricated with above mentioned resin compositions (Movie S2 and Figure S1, Supporting Information). However, in the case of GelMa-BSA-RB resin, the number of cell-attaching and matrix metalloproteinase responsive peptide motifs[35] could not be increased further by increasing the proportion of GelMa without resin gelation at room temperature.
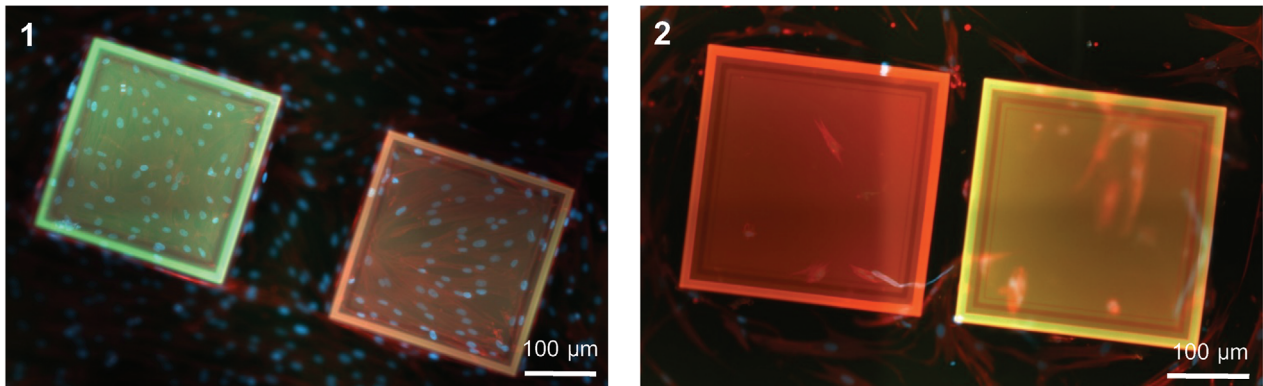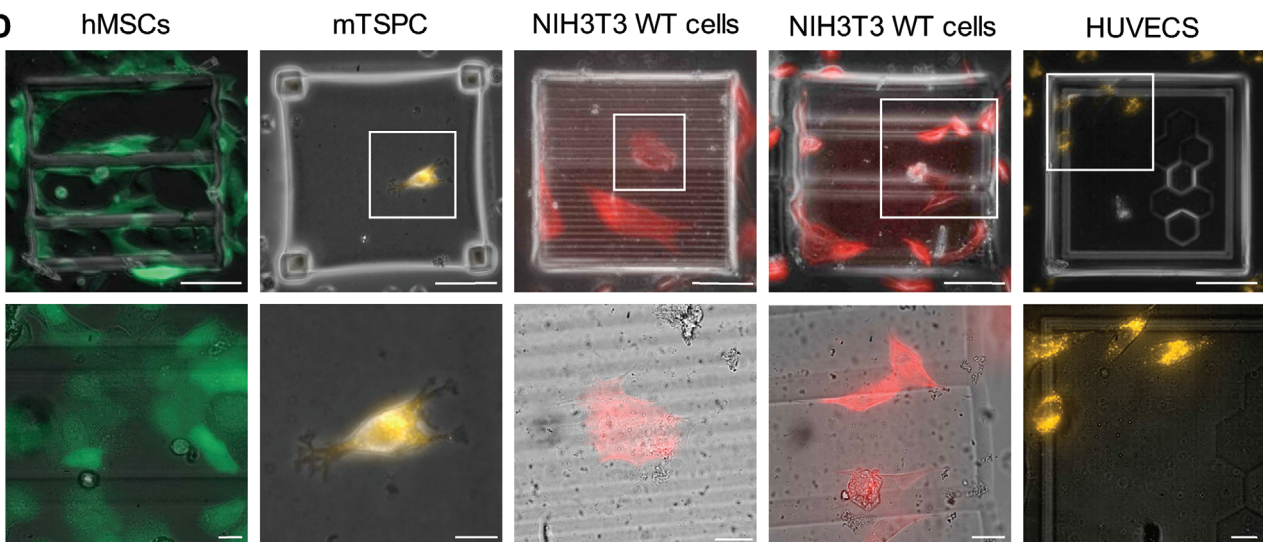
**ADVANCED
SCIENCE NEWS**

www.advancedsciencenews.com

**ADVANCED
HEALTHCARE
MATERIALS**

www.advhealthmat.de

To achieve large-scale gelatin-based high-precision cell scaffolds, we thus explored the highly substituted gelatin derivative GM10[58,59] together with RB as a photo-initiator. This gelatin derived protein is modified to be liquid at room temperature[53] and is therefore suitable for dip-in printing. Such good TPS characteristics of the GM10-RB resin allowed for the fabrication of scaffolds with higher design complexity. Therefore, we inserted a double-layered mesh including 5 µm holes at the top and 2.5 µm holes at the bottom, whereas the posts were arranged in a hexagon layout (Figure 2B, insert). Just as the BSA scaffolds, these were also coated with fibronectin directly after printing. hMSCs were allowed to colonize the high-precision 3D scaffolds for 2.5 days, before they were fixed and stained for their actin cytoskeleton and cell nuclei. A 3D confocal orthoview revealed that the applied cells successfully colonized throughout the entire mesh structure (arrows in Figure 2B). Additionally, we observed cells that attached to the outer scaffold wall perpendicular to the glass surface (arrowheads in Figure 2B) as well as to the glass substrate enclosed by the scaffold (Movie S3, Supporting Information).

Next, by confocal microscopy we observed that phLFs colonized GM10-RB scaffolds coated with fibronectin (Figure 2C1) more efficiently compared to uncoated ones (Figure 2C2). This finding was further corroborated by 48 h live-cell imaging, indicating that a higher number of cells attached to the fibronectin-coated scaffolds. Furthermore, these cells displayed higher migratory activity compared to uncoated controls (Movie S3 and Figure S1, Supporting Information). In agreement with previous studies, we conclude that coating with[13] or an integrated printing of ECM[29] proteins are imminent for the successful colonization of cells in bioprinted 3D scaffolds.

All scaffolds printed with protein-based resins containing RB as photo-initiator displayed a strong inherent auto-fluorescence after sample development that interfered with subsequent fluorescence microscopy. As good fluorescence imaging quality is crucial for biocompatibility assessment, we investigated LAP (Lithium phenyl-2,4,6-trimethylbenzoylphosphinate) as a photo-initiator for GM10 printing to substitute RB. By introducing high protein and photo-initiator concentrations[13,37] of 25 wt% GM10 and 68 mM LAP final concentration and by tuning the laser parameters (laser power and scan speed), we achieved accurate and stable scaffolds for scan speeds ranging from 5 to as high as 95 mm s^{-1} (Figure S2, Supporting Information), which is equivalent to the maximum available galvo-scanner movement in our TPS system. The high cross-linking efficiency of the resin composition is important for further upscaling of the entire workflow and a further reduction of printing times (Table S2, Supporting Information). The biocompatibility of GM10-LAP scaffolds coated with fibronectin was successfully tested by colonization with different cell types: hMSCs, mTSPCs, NIH3T3 WT, HU-VECs and primary human fibroblasts (Figure 2). These cells were colonized on 280 × 280 × 15 µm³ scaffolds with 35 µm high frames and various imprinted geometries (Table S3, Supporting Information, designs D3–D6). Here, hMSCs spread well on scaffolds containing compartments with 100, 75, and 45 µm in width indicating efficient cell adhesion. In contrast, mTSPCs were cultivated on rectangular, free hanging scaffolds, supported by posts at each corner and adhered only in small numbers. Also, NIH3T3 WT cells spread efficiently on scaffolds containing wave patterns (top: 20 µm wavelength, bottom: 10 µm wavelength) and 100, 75, and 45 µm wide compartments. Last, the observed morphology of HUVECs indicated their successful adherence to scaffolds containing hexagonal towers.

Altogether, these results demonstrate the flexibility of high-precision 3D printed structures regarding structure design and successful colonization with various cell types. This strongly suggests that our GM10-LAP biopolymer formulations are highly biocompatible as well as applicable for complex and advanced tissue engineering applications. The outstanding advantage of using LAP as photo-initiator is its optical transparency and low fluorescent background in the visible spectrum (Figure 2D), which is invaluable for imaging and subsequent analysis of fluorescently labeled cells.

2.3. Mechanical Characterization of Biological Microscaffolds with IT-AFM

IT-AFM has been used extensively to characterize native[60,61] and artificial tissue constructs[62,63] and several groups have already reported YM values of biological resin compositions processed with TPS (**Table 1**).[46,52] Here, the TPS printed protein-based scaffolds were indented with a cantilever tip (**Figure 3**A), and the YM was extracted from the resulting force-indentation curve (Figure 3B), as described in the Experimental Section. For the specimen printed with GM10 and LAP with a 25× objective, we were able to detect two distinct sections with different curvatures in the force-indentation curves, indicating two regions of the material with distinct YM. In Figure 3B, an exemplary force-indentation curve with a softer region at ≈0–0.5 µm indentation depth with a YM of 3 kPa, here referred to as interface, and a stiffer bulk material from ≈0.5 µm indentation depth onward with a YM of 26 kPa is displayed. Figure 3C shows the corresponding distribution of YM values of interface and bulk material obtained from 400 measured points within a 20 × 20 µm² area, in two overlaid histograms. Mean YM values (μ) were 1.93 and 20.49 kPa for interface and bulk material, respectively. This finding is in accordance to Roether et al., who described significantly lower local elasticities of proteinaceous, cryogelated scaffolds in comparison to the bulk modulus.[64]

Figure 2. Generation of biocompatible high-precision 3D printed cell scaffolds. A1) A mesh structure with 5 µm holes supported by posts was designed with CAD software, printed in dip-in mode using BSA-RB (green) and seeded with hMSCs. The actin cytoskeleton of hMSCs was stained with ATTO 594 phalloidin (red) and the cells were imaged from three different perspectives: A2) top, A3) side, and A4) bottom. Arrows indicate scaffold orientation in all three spatial directions. Cells can be detected on the top and on the bottom of the scaffold. B) A scaffold with higher design complexity (insert) composed of two stacked meshes and hole sizes of 2.5 µm (bottom mesh) and 5 µm (top mesh) were 3D printed with GM10-RB (pink), seeded with hMSCs and imaged by confocal microscopy ($n = 1$). Arrows indicate hMSCs attached to mesh structures, whereas arrowheads point to hMSCs spreading along the outer scaffold surface. On GM10-RB scaffolds with C1) fibronectin coating we observed increased cell attachment of primary human lung fibroblast (phLFs) compared to C2) uncoated ones ($n = 2$). D) The scaffold geometry can easily be modified and various cell types successfully adhered to GM10-LAP scaffolds showing low auto-fluorescence of printed structures (scale bars top: 100 µm, bottom: 25 µm, each $n = 3$).

**ADVANCED
SCIENCE NEWS**

www.advancedsciencenews.com

**ADVANCED
HEALTHCARE
MATERIALS**

www.advhealthmat.de

Table 1. Literature overview of Young's modulus values of protein-based scaffolds printed with TPS and quantified with AFM. Photo-initiators were methylene blue (MB), flavin adenine dinucleotide (FAD), rose bengal (RB) and lithium phenyl-2,4,6-trimethylbenzoylphosphinate (LAP). Hydrogels were gelatin, silk fibroin, albumin, lysozyme, avidin, poly-(ethylene) glycol-modified hyaluronic acid (PEG-HA-SH), and bovine serum albumin (BSA).

| Young's modulus	Material	TPS Objective	AFM tip	Ref.
2–7 kPa	Gelatin	63× (NA 1.4)	glass spheres (k: 0.05 N m^{-1})	[52]
220.000 kPa	Silk fibroin	60× (NA 1.35)	silicon nitride (k: 42 N m^{-1})	[92]
50–8.000 kPa	Albumin and MB	100× (NA 1.4)	tip-less AFM cantilevers (k: 0.03 N m^{-1}, k: 2.6 N m^{-1})	[51]
600–9.000 kPa	Lysozyme and MB			
200–12.000 kPa	Avidin & MB			
15.9 kPa	PEG-HA-SH	32× (NA 0.85)	n.a.	[93]
500–2.500 kPa	BSA and FAD	100× (NA 1.4)	sphere (radius < 10 nm, k: 0.2 N m^{-1})	[33]
1 500 kPa	BSA and RB	60× (NA 1.0)	(k: 4−6 N m^{-1})	[46]
30 kPa	BSA and RB	40× (NA 1.3)	Tip with plateau ($\approx$1.8 μm) (k: 0.06 N m^{-1})	[94]
100–300 kPa	BSA and RB	63× (NA 1.4) top-down	Four-sided pyramid (k: 0.03 N m^{-1})	This Study
5–10 kPa	BSA and RB	25× (NA 0.8) bottom-up		
20–30 kPa	GM10 and LAP			
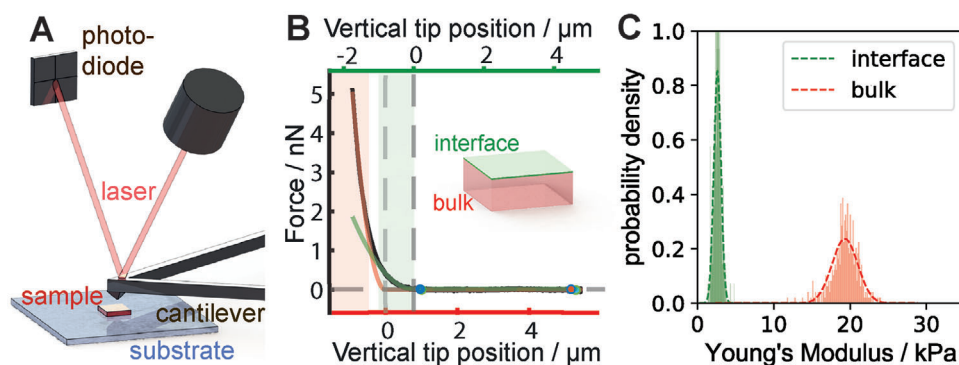
Figure 3. Indentation type AFM workflow to analyze the Young's Modulus (YM) of microscaffolds. A) Schematic of an AFM setup: A cantilever tip is probing a protein-based cell scaffold on the substrate. B) The cantilever deflection is recorded through a reflected laser beam on a segmented photodiode and converted to force-indentation curves. Our microscaffolds printed with GM10-LAP were best fitted by combining two fit curves, indicating a stiffer bulk regime for 0.5–2 μm indentation depths and a softer interface region at the print surface ($n = 3$). C) Plotting all measured YM values of the bulk material within the sampled region revealed a homogeneous spatial distribution which can be plotted as a histogram.

We also used IT-AFM to determine the influence of various 3D printing parameters on resulting protein scaffold YM (**Figure 4**). For this, BSA-RB as a TPS benchmark (white) and our GM10-LAP resin (grey) were tested regarding their reproducibility and stability as well as the influence of fabrication parameters and post-processing with the natural cross-linker genipin on their respective YM. Test scaffolds were printed in dip-in mode with a 25× objective from GM10-LAP resin. The mean YM values (μ) of the bulk within measurement series of each 100, 400, and 1600 points, all obtained from the same scaffold, were 21.3, 21.9, and 22.2 kPa. They showed a maximal deviation of 0.9 kPa and a maximal standard deviation (σ) of 2.0 kPa (Figure 4A). Comparing four different measurements obtained from four different positions within one scaffold revealed mean YM values of the bulk of 21.4, 21.5, 20.5, and 21.3 kPa and a maximum standard deviation of 1.2 kPa (Figure 4A, positions). For BSA-RB resin printed bottom-up with a 63× objective, we tested the stability of the

bulk's YM of TPS printed samples over the course of 7 days. 1 day after printing (day 1) these samples had a mean YM of 97.9 kPa. The mean YM of samples stored in cell culture medium containing Dulbecco's Modified Eagle Medium (DMEM) supplemented with 1% penicillin-streptomycin, 10% fetal calf serum and 1% GlutaMAX at 37 °C and 5% CO_2 for 7 days was 103.7 kPa (Figure 4A, cell culture conditions). In respect to the standard deviation of $\approx$22 kPa, the YM of these samples remained stable over the course of 7 days. In comparison, a decrease of the bulk's YM was observed for samples stored in phosphate-buffered saline (PBS) at 4 °C from initially 97.9 kPa at day 1 over 65.0 kPa at day 2 to 47.0 kPa at day 7 (Figure 4A, PBS).

To investigate the influence of the fabrication parameters on the mechanical properties of high-precision 3D-printed scaffolds, we varied scan speed, laser power, number of laser passes and objective magnification and quantified the YM for all parameter settings tested. The top graph in Figure 4B (scan speed and laser

A reproducibility and stability
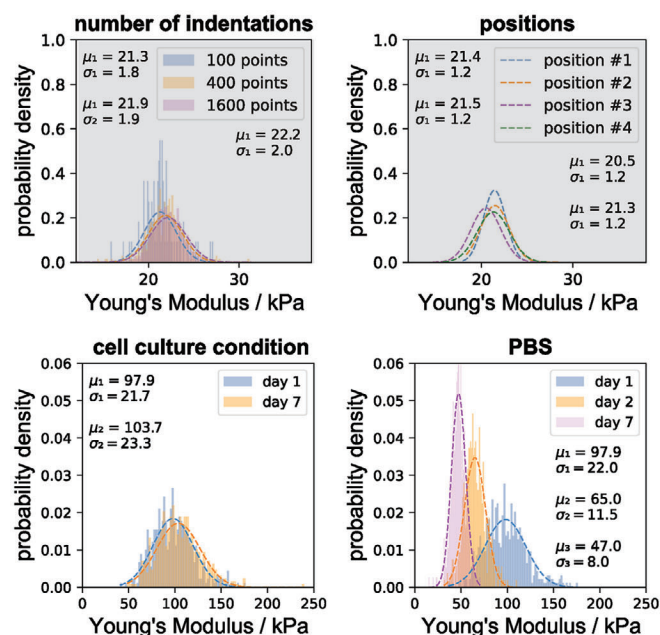
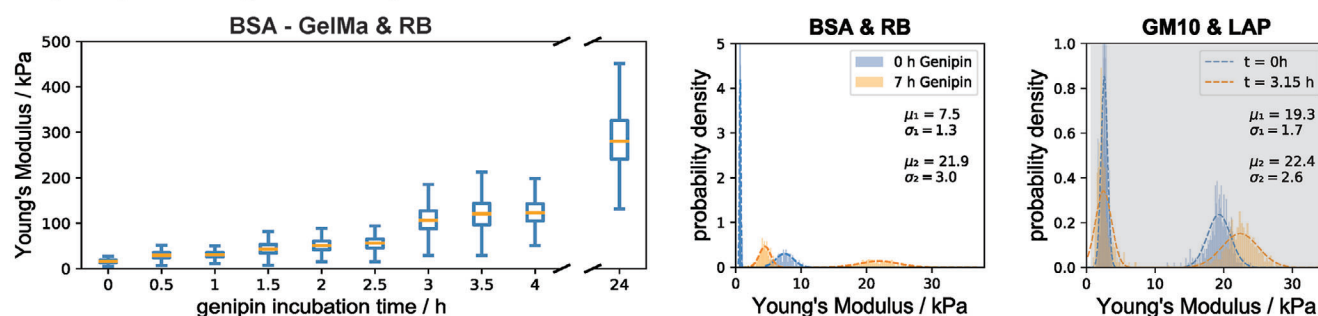## B fabrication parameters
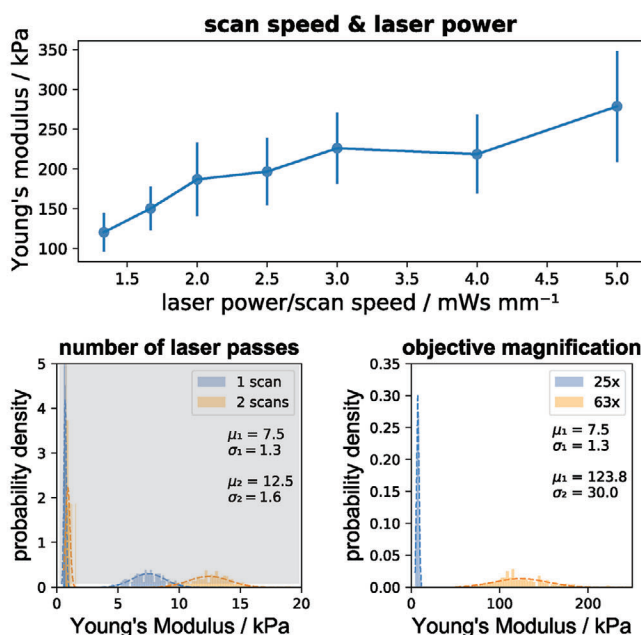
C post-processing with Genipin

Figure 4. Impact of the 3D printing process on the Young's modulus (YM) of protein-based high-precision scaffolds quantified by IT-AFM. AFM measurements performed on 3D printed scaffolds fabricated with TPS using BSA-RB (white) and GM10-LAP (grey) resin compositions. Histograms display mean values (μ) and standard deviations (σ) of the YM. A) AFM-based YM quantification is robust in a range of 100 to 1600 measurement points per sample and at different measurement positions within one sample. The temporal stability of samples when stored in cell culture conditions and in PBS at 4 °C was also examined. B) Fabrication parameters, including number of repeated laser passes, laser power, and scan speed, as well as objective magnification, influence the protein-scaffold's YM and hence require careful optimization to attain desired YM values. C) Post-print chemical crosslinking using genipin can be used to increase the scaffold's YM. The density of additional cross-linking with genipin is sensitive to the protein-based resin. Additional details regarding individual samples, measurement replicates and indentation depths are listed in Table S4, Supporting Information.

power) summarizes our findings regarding scan speed and laser power and displays the observed YM values as a function of deposited laser energy per length. The standard deviation is displayed as error bars. As expected, we achieved an increase in the mean YM for increasing laser power and decreasing scan speed ranging from 120.4 kPa ($\sigma = 24.3$ kPa) at 40 mW laser power (LP) and 30 mm s^{-1} scan speed (SS) to 278.6 kPa ($\sigma = 69.68$ kPa) at 50 mW LP and 10 mm s^{-1} SS. Furthermore, the scaffold's YM was sensitive to multiple laser exposures of the geometry. For GM10-LAP resin (gray), exposing the scaffold geometry twice led to an ≈5 kPa increase of the bulk's YM from 7.5 to 12.5 kPa. With 0.9 kPa, the YM of the interface region increased by 0.22 kPa and remained softer than the bulk region. Hence, while the bulk YM

increased by 66.6 % with the second laser scan, the YM of the interface region increased only by 32.9 % (Figure 4B, number of laser passes). Also, the choice of objective magnification had a major impact on the mechanical properties. For BSA-RB resin (white) printed with a 25× objective in dip-in mode we measured a bulk YM of 7.5 kPa, in comparison to 123.8 kPa for scaffolds printed with a 63× objective in bottom-up mode. For increasing YM, associated standard deviation increased up to 23-fold (Figure 4B, objective magnification).

The mechanical properties of the scaffolds can not only be adjusted by the printing parameters, but also by applying additional cross-linking agents post-printing. We determined the time-dependent increase in YM during incubation at room tem-

**ADVANCED
SCIENCE NEWS**

www.advancedsciencenews.com

**ADVANCED
HEALTHCARE
MATERIALS**

www.advhealthmat.de

perature when incubating with 10 mM of the cross-linker genipin for a range of resin compositions (Figure 4C). IT-AFM measurements were continuously carried out during genipin incubation on a given sample. The most significant YM modulation occurred on BSA scaffolds containing 20% GelMa, where it increased from initially 15.5 kPa (σ = 4.6 kPa) to 288.7 (σ = 75.9 kPa) after 24 h incubation, constituting a 270 kPa or almost 20-fold increase. For GM10-LAP (gray) and BSA-RB (white) resins, the increase during post-cross-linking was far less efficient. We observed an increase of the mean YM of the bulk region from 7.5 to 21.9 kPa on BSA-RB scaffolds after 7 h of genipin incubation and from 19.3 to 22.4 kPa on GM10-LAP scaffolds after 3.15 h.

Our IT-AFM results showed 100 measurement points to be sufficient for conclusive YM determination, since the mean YM obtained from 1600 points only diverged by 3%, which we found to be insignificant. Observing deviations of protein-based scaffold mechanics over time can reveal information about the aging of cross-linked hydrogels and can, therefore, indicate degradation processes or swelling.[64] This is especially important to consider when conducting cell experiments over several days or weeks. BSA-RB scaffolds stored in cell culture conditions were stable, while a softening was observed when stored in PBS at 4 °C (Figure 4A). Mechanical properties of protein-based hydrogels also depend on the fabrication parameters (Figure 4B). By increasing the numerical aperture and magnification of the objective, the voxel size decreases resulting in higher laser intensities and higher numbers of cross-linking events within the polymerizing voxel.[65] Note that because of the two-photon absorption mechanism of the photo-initiator, the resulting cross-linking density depends on the laser intensities in a highly non-linear way.[66] A higher cross-linking density ultimately results in a more rigid polymer network with higher YM values. In addition to increasing the YM by enhancing laser exposure, the YM can also be increased by introducing additional cross-links post printing, such as by the incubation with genipin (Figure 4C). This facile adjustment of scaffold YM during and after TPS fabrication may be used to locally adapt scaffolds to specific cellular requirements to deliberately guide cellular maturation and functions. In addition to batch to batch variations of resin components, the storage conditions of samples and the time between printing and measurement may have a significant impact on obtained results. Print settings such as laser power, scan speed, objective magnification, and the number of subsequent laser scans have a major influence on mechanical properties of the protein-based scaffolds and should, therefore, be considered when comparing such values.

2.4. Tunable High-Precision Scaffolds for Myoblast Actin Fiber Alignment and Lung Fibroblast Colonization of In Vivo Derived 3D-Topographies

3D printed scaffolds with defined mechanical properties have been designed to guide cellular growth and differentiation,[67] and substrate topography can stimulate actin filament alignment within single cells[68] and enhance tissue maturation.[69] While it has been shown that both the rigidity and the shape of the ECM influences cell development, both aspects have not yet been optimized within the same in vitro assay. TPS is a versatile tool

to print high-precision 3D scaffolds with a high freedom in design regarding a desired topography and rigidity. Thus, this fabrication method is capable of generating high-precision scaffolds with tunable YM and geometries. The immortalized mouse myoblast cell line (C2C12) is a widely used model to study the biomechanics of single cells[70,71] and differentiating tissues[72] on substrates that mimic the ECM in natural conditions of myocytes (YM ≈ 12 kPa).[73] Regulation and maintenance of muscle mass is facilitated by the differentiation of skeletal muscles to myotubes and an optimal muscle function is accompanied by the alignment of actin filaments. C2C12 can proliferate, form confluent tissues and differentiate into myotubes under the right cell culture conditions in vitro.[68,74,75] Using actin filament orientation maps (AFOM), which color code the actin filament alignment angles, we used our protein-based TPS scaffolds to show that 3D spatial confinement and substrate topography together with natural mechanical matrix properties (rigidity) enhance actin alignment.

Figure 5A shows a typical confluent C2C12 cell layer cultured on a glass substrate without tissue specific topography and YM (YM$_{glass}$ ≈ 50 GPa). The cellular actin cytoskeleton was stained with Alexa 594 phalloidin, the nuclei appear blue by DAPI staining. While individual clusters of cells formed well-aligned actin filaments, a strong diversity of cell alignment was observed on a larger scale due to missing guidance of the ECM on the glass substrate, as illustrated by the respective AFOM (Figure 5B). To investigate cells under topographical constraints, we colonized C2C12 cells on high-precision 3D scaffolds with designs containing compartments or fine wave patterns (Table S3, Supporting Information (D4 and D5)). The scaffolds were printed with GM10-LAP resin in the dip-in setup. The individual compartments within these scaffolds were 100, 75, and 45 μm wide and 300 μm long and were thus equal to or greater than the size of an individual adhered cell. The second design included wave patterns with wavelengths of 10 and 20 μm and these patterns were extruded over the length of 300 μm. The actin alignment was quantified using the nematic order parameter <S>. While <S> = 1 states perfect alignment of all filaments, <S> = 0 states homogeneously distributed filament directions. Here, we found that <S>, which corresponds to actin filament alignment, increased with increasing width of the chambers imprinted on 3D scaffolds (Figure 5C). While the width of the spatial confinement clearly dictated cell alignment, it was possible to increase the spatial alignment by altering the substrate topography. Figure 5D shows a 300 × 300 μm² scaffold chamber, expecting <S> ≈ 0. However, an order parameter of <S> = 0.33 was obtained due to the wave-patterned substrate topography. While this topography triggered actin filament alignment, no significant difference in <S> was observed between the top (10 μm wavelength) and bottom part (20 μm wavelength) of the scaffold. Yet, the cells in the bottom part of the chamber lead to a narrower filament alignment distribution, as shown by the histograms. This could indicate an enhanced effect for filigree patterned substrates below the single cell size of adhered cells. The optical analysis of actin fiber orientation on high-precision 3D scaffolds was only possible because of the low auto-fluorescence of the GM10-LAP resin.

To demonstrate cell colonization on fabricated 3D microscaffolds, an excerpt of in vivo mouse lung parenchymal tissue containing entire alveoli was printed with TPS with GM10 and LAP
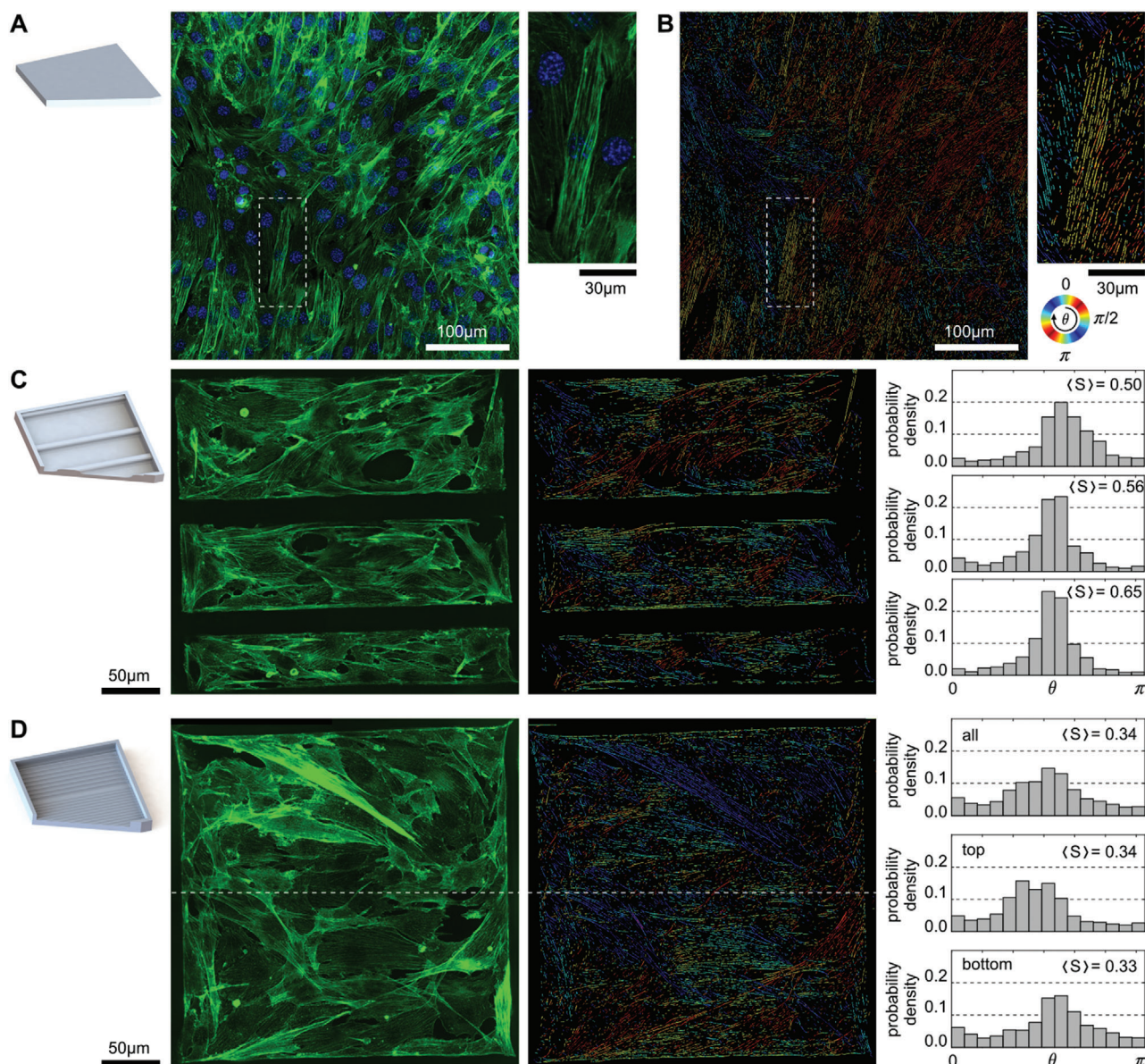
Figure 5. Scaffold topography confers growth phenotypes of mouse muscle cells. A) Confluent C2C12 cell layer without spatial confinement on glass. Shown are actin filaments (green) and nuclei (blue). The right image shows a close up of the left image (white dashed line). B) Actin orientation quantification map of images shown in (A). Color coding indicates actin filament orientation angle, θ. C,D) Cellular response to spatial confinement in GM10-LAP scaffolds. From left to right: 3D rendered chamber illustration, actin filament stained cell layer ($n = 1$), actin orientation quantification map, and the respective probability density distributions quantified with the nematic order parameter $<S>$. C) Cell layers in compartments with different widths (top: 100 µm, middle: 75 µm and bottom: 45 µm). D) Cells on scaffolds with two different wave-pattern substrates (top: coarse wave pattern with 20 µm wavelength; bottom: fine wave pattern with 10 µm wavelength).

(grey), and subsequently coated with fibronectin (**Figure 6**). The print template was extracted as 3D mesh from confocal image stacks, as previously described in Section 2.1 (Figure 1A). phLFs were colonized on scaffolds for 96 h and stained with ALEXA 594 phalloidin (red) and DAPI (white) after fixation. Again, confocal 3D fluorescence imaging of an excerpt of a 888 × 888 × 104 µm (4 × 4 prints, each with 222 × 222 × 222 µm, $n = 3$) printed scaffold produced an orthoview (Figure 6A) and a 3D rendered volume (Figure 6B and Movie S4, Supporting Information), which both clearly revealed a spatial 3D distribution of colonized cells.

Strikingly, the partially observed flat and round morphologies of pHLFs found in alveolar areas were highly reminiscent to morphologies of fibroblasts found in recolonized decellularized 3D ex vivo lung tissue scaffolds (Figure 6C).[41]

3. Conclusion

Functional tissue is based on the interaction of numerous factors including tissue architecture, mechanics, and biochemical factors. All these stimulate organotypic cellular dynamics.
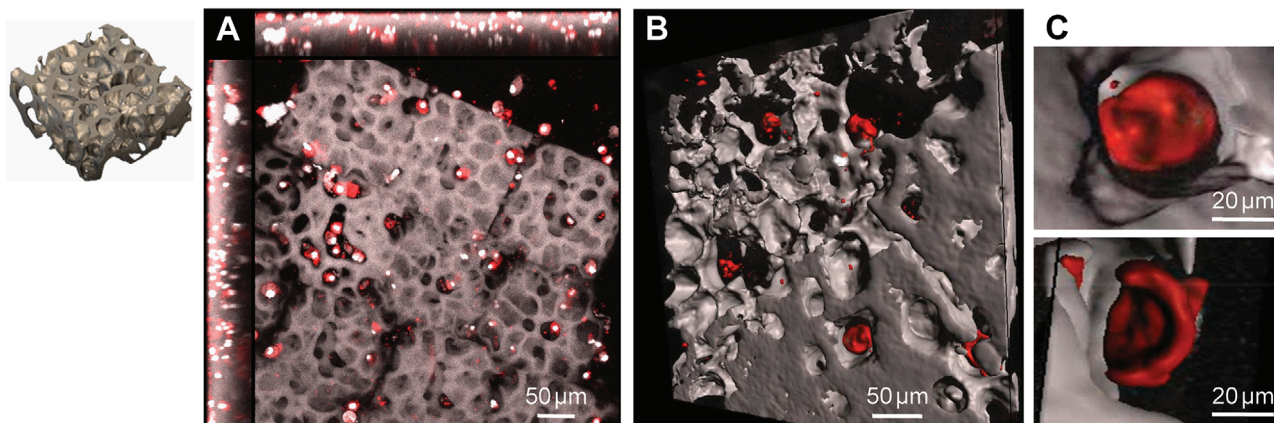
**ADVANCED
SCIENCE NEWS**
www.advancedsciencenews.com

**ADVANCED
HEALTHCARE
MATERIALS**
www.advhealthmat.de

Figure 6. 3D printed alveolar scaffolds colonized with primary human lung fibroblasts (phLFs). Alveolar in vivo tissue geometry printed with TPS using GM10 and LAP colonized with phLFs for 3 days and stained for the actin cytoskeleton with ALEX 594 phalloidin (red) and cell nuclei with DAPI (white). A) An orthoview of a stitched patch containing a 4 × 4 array of 222 × 222 × 104 µm scaffolds, clearly showing a 3D distribution of colonized cells in the fabricated lung microstructure ($n = 3$). B) 3D rendering of a confocal z-stack shown in (A) and (C) close up images of pHLF cell morphology in alveolar regions.

To further unravel these complex cell-ECM interactions in 3D, we need fabrication methods that provide precise control of the contributing factors, such as topography, biochemical composition (e.g., adhesion sites) and Young's modulus on the micrometer scale.

Here, we demonstrated a dip-in setup for TPS using a humidified printing chamber to fabricate protein-based scaffolds up to mm sizes. We introduced a GM10-LAP resin formulation to remove auto-fluorescence, which is essential for high-resolution 3D fluorescence imaging of cell-scaffold interaction. These fabrication method improvements allowed us to fabricate and colonize scaffolds with various cell-lines, including myoblast on alignment substrates and lung fibroblasts on in vivo derived 3D-topographies. Through IT-AFM we confirmed that resulting scaffold's Young's moduli are in the range of 7–300 kPa, matching those of many biological tissues. However, numerous experimental details of the fabrication process, storage conditions, and even storage time can profoundly affect resulting Young's moduli. Engineering novel resins or even negligible process revisions, such as introducing a new cell culture medium, should hence be stringently validated.

High-resolution, non-destructive microscopy of ever larger 3D tissue segments, imaged by advanced microscopy[76] or microCT[77] will provide detailed geometric instruction for more complex microtissue replicas in the future and will also be essential for monitoring tissue maturation on such 3D printed scaffolds. A printed perfusion system mimicking the vasculature may supply such tissue replicas with nutrients to facilitate long-term cultivation.[24] Also, a combination of several resins can allow for multi-material,[33,78] protein-based scaffolds selectively adapted to individual cell preferences within co-cultures. These include a systematic permutation of the Young's modulus within a geometry. Spatially detailed bio-mechanical information from IT-AFM or Brillouin microscopy[79] will increasingly inform on how to optimize in vitro ECM rigidities.

TPS is a powerful tool to fabricate scaffolds mimicking the extracellular matrix in its geometrical, biochemical, and physical properties. Nevertheless, this method is bound by the trade-off between accuracy and printing speed which impedes the fabrication of large scaffolds while maintaining a high resolution. Further tuning resin chemistry such as the photo-initiator[95] and improved TPS instrumentation will increase fabrication rates of protein-based resins to eventually print full organs at the desired resolution in a high-throughput process.[80]

To ultimately recreate the ECM in all its essential biological details as an in vitro experimental platform requires careful optimization of all relevant details. These include high spatial resolution in geometry, mechanics and biochemistry, constant quality control of fabricated structures, non-destructive high-resolution 3D imaging, and non-destructive monitoring of the maturation processes. Given the interdisciplinarity nature of this task, a platform similar to the protein data bank or the human cell atlas, could accelerate the development of such functional microtissue, by expanding and integrating available multiscale information including spatial proteomics and genomics data.[81,96] Such a common resource could facilitate downstream analysis via common-vetted algorithms, as well as automated visualization pipelines.

4. Experimental Section

Unless stated otherwise, all chemicals and cell culture reagents were purchased from Sigma-Aldrich (St. Louis, MO, USA).

Hydrogel resins—RB Photo-Initiator Preparation: 85mM RB was prepared by dissolving RB (>95% purity) in ddH$_2$O. The solution was centrifuged for 5 min at 13×10^3 rpm to sediment undissolved impurities.

Hydrogel resins—LAP Photo-Initiator Preparation: Lithium phenyl-2,4,6-trimethylbenzoylphosphinate (LAP) with >95% purity was dissolved in PBS to prepare a stock solution with a final concentration of 340 mM, yielding a milky suspension. The nominal solubility of LAP is of order 100 mM and full solubilization is only achieved after admixing LAP stock to the protein resin.

Hydrogel resins—BSA Resin Preparation: Lypholized Bovine Serum Albumin (>98% powder) was dissolved in 20 mM 4-(2-hydroxyethyl)-1-piperazineethanesulfonic acid (HEPES) containing 15.4 wt% dimethyl sulfoxide (DMSO) to a final concentration of 40 wt% and stored at 4 °C until further processing. The hydrogel solution was vortexed for 5 h until BSA

**ADVANCED
SCIENCE NEWS**

www.advancedsciencenews.com

**ADVANCED
HEALTHCARE
MATERIALS**

www.advhealthmat.de

was fully dissolved. Final BSA-RB resin was obtained by mixing selected BSA stock solution with RB stock solution in the ratio 9:1 and immediately used for 3D printing.

Hydrogel resins—GelMa Hydrogel Preparation: Gelatin methacryloyl (gel strength 300 g Bloom, degree of substitution 60%) was dissolved in PBS solution (Dulbeco, w/o Ca²⁺, w/o Mg²⁺, Biochrom GmbH) while heating to 30 °C to a final concentration of 25 wt%. For final resin composition, GelMa stock solution was mixed with RB stock solution at a 9:1 (GelMa-RB). Alternatively, GelMa:BSA 1:4 protein stock solution was mixed with RB stock in the same 1:9 ratio (BSA&GelMa-RB). This equated to final concentrations of 22.5 wt% GelMa or 4.5 wt% GelMa and 28.8 wt% BSA, respectively.

Hydrogel resins—GM10 Preparation: Gelatin methacryloyl was synthesized and characterized as previously described using gelatin type B (Limed, bovine bone, 232 g Bloom, viscosity: 4.5 mPa s, Gelita, Germany), yielding GM10 with a degree of methacrylation of 1.07 mmol g⁻¹.[58] GM10 was dissolved in PBS and mixed with LAP stock for final concentrations of 25 wt% GM10 and 68 mM LAP photo-initiator (GM10-LAP).

High-Resolution 3D Printing: All 3D cell scaffolds were fabricated by converting STL files to print job instructions using Describe followed by selective exposure carried out with the Nanoscribe GT Photonics Professional operating in dip-in mode using protein-based resins equipped with an erbium-doped femtosecond laser source with a center wavelength of 780 nm and a power of about 150 mW and a 25× (NA 0.8) or 63× (NA 1.4) objective (all Nanoscribe GmbH). All prints for cell culture were carried out in 35 mm petri dishes (MatTek) each containing an embedded, 160–190 µm thick glass slide (No. 1.5) in the center of the dish. The bottom side of the petri dish was taped onto the bottom side of the substrate holder with double-sided adhesive tape. Thus, the petri dish was circumferentially aligned with the circular notch of the substrate holder. The flexible water reservoir was designed in CAD software SolidWorks (Dassault Systèmes, 2017) to fit objective and petri dish dimensions, and printed with a Form2 3D printer using the flexible resin (both Formlabs GmbH). AFM samples were printed onto 170 µm thick, 22 × 22 mm glass substrates. Prints were thoroughly rinsed with PBS to remove unpolymerized resin and subsequently stored in PBS containing 1% penicillin-streptomycin at room temperature.

Cell Handling: Unless stated otherwise, all cells were handled as follows: Cells were cultured in DMEM (BS.FG 0445, Bio&SELL GmbH) supplemented with 1% penicillin-streptomycin (BS.A 2213, Bio&SELL GmbH), 10% fetal calf serum (F7524-500mL, Sigma-Aldrich Chemie) and 1% GlutaMAX (35 050 038, Life Technologies GmbH) under humidified conditions at 37 °C and 5% CO₂. Medium was changed every 2–3 days and cells were passaged at 80–90% confluency using 0.5% trypsin-EDTA solution (BS.L 2163, Bio&SELL GmbH), centrifuged at 500 rpm for 5 min at room temperature and finally seeded in a ratio of 1:5 or 1:6 in T175 cell culture flasks (83.3912.002, Sartstedt AG und Co.). Deviations were made for following cell lines:

Cell Handling—Primary Cell Culture and Human Tissue and Ethics Statement: Primary human lung fibroblasts (phLFs) were isolated by outgrowth from human lung tissue derived from lung explants or tumor-free areas of lung resections. Cells were cultured in Dulbecco's Modified Eagle Medium F-12 with 20% (v/v) special processed fetal bovine serum (PAN Biotech) and 100 International Units Penicillin per mL and 100 µg per mL Streptomycin. Cells were used for experiments until passage 7. Human biomaterial and clinical data was kindly provided from the CPC-M bioArchive and its partners as the Asklepios Biobank Gauting, the Klinikum der Universität München and the Ludwig-Maximilians-Universität München. Participants provided written broad consent to participate in this study, in accordance with approval by the local ethics committee of the LMU, Germany (Project 333-10, 454-12).

Cell Handling—NIH3T3 WT: Lifeact-RFP expressing (rLV-Ubi-LifeAct Lentiviral Vectors, ibidi GmbH) murine NIH3T3 fibroblast wildtype (WT) cells were kindly provided by Prof. Christof Hauck and Timo Baade (University of Konstanz). Cells were cultured in DMEM growth medium (Biochrom) supplemented with 10% fetal calf serum (FCS) (Biochrom), 1% GlutaMax (Gibco) and 1% Penicillin/Streptomycin (Biochrom) at 37 °C and 10% CO₂ in a humidified cell culture incubator.

Cell Handling—mTSPC: Mouse tendon stem/progenitor cells originally isolated from WT and Tnmd KO tail tendons at 6, 9, 12, and 18 months of age[82,83] were kindly provided by Prof. Dr. Denitsa Docheva and Manuel Delgado Cáceres (University of Regensburg). mTSPC were cultured in DMEM/HAMs F-12 (Biochrom F4815) supplemented with 1% GlutaMAX (Thermo Fisher Scientific), 10% fetal bovine serum (Biochrom), 1% Non-essential amino acids (REF 11140-035, gibco), 1% Penicillin/Streptomycin (Biochrom) and ascorbic acid 2-phosphate (5.8 mL of 36 mg mL⁻¹).

Cell Handling—C2C12: Mouse myoblast cells (<20 passages, Sigma-Aldrich) were cultured in DMEM (D6046, Sigma-Aldrich) supplemented with 10 wt% fetal bovine serum (F4135, Sigma-Aldrich), and 1% penicillin-streptomycin (P0781, Sigma-Aldrich) under humidified conditions at 37 °C and 5% CO₂. The cells were treated with trypsin to enzymatically cleave their adhesion proteins to detach them from the culture flask as well as from each other, using trypsin–EDTA solution (0.25%, T4049, Sigma). Cells were cultured 2–4 days until confluency was reached.[70,84]

Cell Handling—HUVEC: Human Umbilical Vein Endothelial Cells (HUVEC, pooled donors, cryopreserved, C-12203) and respective growth medium (Endothelial Cell Growth Medium 2) were obtained from PromoCell GmbH.

Cell Handling—Scaffold Seeding: Scaffolds were coated with 50 µL of 100 µL mL⁻¹ fibronectin (AppliChem GmbH) for 30 min at room temperature to improve cell adherence. After washing with PBS, petri dishes were filled with 2 mL DMEM (D6046, Sigma-Aldrich) and seeded with 100–500 µL of cell suspension with a concentration of 5×10^6 cells mL⁻¹.

For muscle tissue constructs, fibronectin from human plasma (300 µL, 5 µg mL⁻¹, Sigma) was applied to the substrates, and allowed to react for at least 3 h at 37 °C prior cell seeding. Thereafter C2C12 cells were counted and seeded with a cell density of 1.6×10^4 cells µm⁻² onto fibronectin-coated substrates.

Cell Handling—Cell Staining: Colonized scaffolds were fixed with 3.7% or 4% PFA for 15 min (37% paraformaldehyde, CP10.1 Carl Roth GmbH + Co. KG), rinsed with PBS, permeabilized with 0.1% Triton-X-100/PBS (Sigma Aldrich, Lot. SLBM1396V/Lot. SLBM1396V) for 2–10 min, again rinsed with PBS and then stained with 10% ATTO 594 phalloidin/PBS (ATTO-TEC, Lot. SA02T25F8) for 15 min at or Alexa 594 phalloidin 1h at room temperature (dark) and 10% DAPI (AppliChem, Lot. 7QD13667) for 15 min. Scaffolds were then rinsed with PBS between each work step and rinsed three times after staining and coated with a drop of Abberior Mount Solid Antifade (Abberior, Lot. MM-2013-2 × 15 mL). All procedures were conducted at room temperature. For staining of C2C12 cells, cell-loaded scaffolds were quenched with 1 M Glycine in PBS for 5 min after fixation with PFA and blocked with 5% FCS in PBS for 30 min after permeabilization. Additional DAPI staining: DAPI (5 mg mL⁻¹ stock; final concentration 300 nM) was added during the last washing step and incubated for 5–10 min at RT. Thereafter, probes were rinsed three times with PBS.

Imaging: Bright-field and fluorescence imaging of hMSCs, HUVECs, mTSPCs, and NIH3T3 WT cells was conducted with AxioObserver.Z1 (Zeiss) and digitalized with ZEN blue software (Zeiss, 2009). During time lapse, cells were kept in respective medium in humidified conditions at 37 °C and 5% CO₂ in a PM S1 incubator chamber (Carl Zeiss) or Incubator PS compact with heating incubation insert (Pecon GmbH). Time-lapse images in various intervals were acquired by using an EC Plan-Neofluar DICI 10× (NA 0.3, Carl Zeiss) objective.

The confocal z-stack of the fixed mesh-like structure containing hMSCs as well as C2C12 cells were imaged with an inverted confocal Spinning Disk Microscope (Zeiss AxioObserver SD) equipped with Yokogawa CSU-X1 Spinning Disk UnitFastScan Confocal Fluorescence Microscope, using 20× (ZEISS Plan-APOCHROMAT 20×, NA 0,8) and 40× objectives (ZEISS Plan-APOCHROMAT 40×, NA 1,4 Oil Dic (UV) VIS–IR) and an EMCCD camera (Photometrix Evolve 512). DAPI was excited with a 405 nm diode laser combined with a 450/50 nm emission filter, Alexa594 was excited with a 561 nm diode laser combined with a 600/50 nm emission filter. Image tiles of up to 4 × 4 with a 10% overlap were recorded and reconstructed using ZEN (Vers. 2.3). For tiled images the ImageJ BaSiC shading correction plugin was applied (Figure S3, Supporting Information).[71]

**ADVANCED
SCIENCE NEWS**

www.advancedsciencenews.com

**ADVANCED
HEALTHCARE
MATERIALS**

www.advhealthmat.de

Atomic Force Measurements: A measure for the stiffness of a material is the YM, which is the ratio of the applied uniaxial stress (σ) and the resulting strain (ϵ). In IT-AFM, the material is indented with a small tip positioned at the end of a cantilever spring. The resulting deflection of a laser beam which is reflected from the backside of the bent cantilever can be detected by a segmented photodiode. Using this quantified beam deflection, the force needed to indent the material to a certain extent can be calculated and plotted as a force-indentation curve. By applying a fit model of the modified Sneddon–Hertz[85] to the obtained force-indentation curves, YM can be estimated. Here, AFM indentation measurements were performed using an MFP-3D Bio (Asylum Research, Oxford Instruments, Goleta, CA, USA) on printed blocks measuring 90 µm × 90 µm × 11 µm. Structures fabricated from varying hydrogel resin compositions were printed on glass coverslips and fixed on objective slides with thermostable wax. AFM indentation experiments were carried out in PBS at room temperature using MLCT cantilevers (Bruker Corporation, Billerica, MA, USA; Cantilever D) with a nominal spring constant of 0.03 N m^{-1}. GM10-LAP measurements were performed by 20 × 20 force-distance curves recorded in a 20 × 20 µm scan area, at a z-piezo velocity of 8 µm s^{-1}, if not stated otherwise. A sampling rate of 25 kHz, a 2 V trigger point and a full z-piezo travel distance of 6 µm was used. For BSA-RB measurements the z-piezo velocity was reduced to 5 µm s^{-1} at a sampling rate of 3.5 kHz, full z-piezo travel distance to 5 µm and 16 × 16 points were measured on a 40 × 40 µm surface. The Young's modulus was derived from the indentation part of the curves, as described previously.[47,86] The actual cantilever force constant was determined for each cantilever individually, using the thermal noise method.[87] Data acquisition was performed with the Igor Pro software (version: 6.3.7.2) and the data analysis with custom-made MATLAB scripts (Mathworks).[88] Histograms were plotted in Spyder (version 4) using python 3.7. Mean Young's modulus values (μ) and standard deviations (σ) of all data points were calculated. For visualization, a Gaussian curve defined by μ and σ was plotted. For additional cross-linking, scaffolds where incubated in10 mM Genipin (>98% HPLC powder, Sigma, G4796) dissolved in PBS.

Actin Filament Orientation Maps: Actin filament stained confocal images of C2C12 tissues were used to calculate actin filament orientation maps using a custom MATLAB script (Mathworks) following previous studies on single cells.[70,89,90] Original images were convoluted with elongated Laplace of Gaussian (eLoG) kernels, which were obtained by convolving a Laplacian filter 0,−1,0; −1,+4,−1; 0,−1,0] and $n = 15$ differently rotated anisotropic Gaussians ($\sigma_x = 3\sigma_y = 1$). The maximum response images were calculated for each pixel, as

$$I_{max}\ (n, x, y) = \max[eLoG\ (n) \times I\ (x, y)]$$

Thereafter I_{max} was processed by the binarized original images using the Otsu's thresholding method.[91] Fibers of the same rotational direction with less than 7 pixels were removed. The obtained images were colorized with a color scheme that corresponds to the local actin orientation angles, θ_n. From each actin filament orientation map the nematic order parameter was calculated, as

$$\langle S \rangle\ =\ \langle \cos 2\ (\theta_n - \theta_0) \rangle$$

where θ_0 is the reference angle, here chosen as 90 degree that corresponds to the direction of the wave pattern.

Statistical Analysis: Scaffolds mimicking alveolar tissue were printed in dip-in mode and seeded with phLFs ($n = 25$).

AFM Data: 98 to 1002 independent measurements were obtained from one to two samples (s) per condition with an indentation depth in the range of 0–2 µm. Curves with a coefficient of determination (R^2) below 0.9 were disregarded. Additional information concerning numbers of individual samples, individual measurements and indentation depths is included in Table S4, Supporting Information.

Data acquisition was performed with the Igor Pro software (version: 6.3.7.2) and the data analysis with custom MATLAB script.[88] Histograms were plotted in Spyder (version 4) using python 3.7.

Actin Filament Orientation Maps were obtained on one sample each and evaluated with MATLAB. Controls consisted of three samples.

Supporting Information

Supporting Information is available from the Wiley Online Library or from the author.

Conflict of Interest

The authors declare no conflict of interest.

[1] M. Seeger, A. Karlas, D. Soliman, J. Pelisek, V. Ntziachristos, *Photoacoustics* **2016**, *4*, 102.

[2] Z. Wu, T. Rademakers, F. Kiessling, M. Vogt, E. Westein, C. Weber, R. T. A. Megens, M. van Zandvoort, *Methods* **2017**, *130*, 79.

[3] W. Liu, Y. S. Zhang, M. A. Heinrich, F. De Ferrari, H. L. Jang, S. M. Bakht, M. M. Alvarez, J. Yang, Y. C. Li, G. Trujillo-de Santiago, A. K. Miri, K. Zhu, P. Khoshakhlagh, G. Prakash, H. Cheng, X. Guan, Z. Zhong, J. Ju, G. H. Zhu, X. Jin, S. R. Shin, M. R. Dokmeci, A. Khademhosseini, *Adv. Mater.* **2017**, *29*, 1604630.

[4] C. Y. Kuo, T. Guo, J. Cabrera-Luque, N. Arumugasaamy, L. Bracaglia, A. Garcia-Vivas, M. Santoro, H. Baker, J. Fisher, P. Kim, *J. Biomed. Mater. Res., Part A* **2018**, *106*, 1476.

[5] M. C. Kim, Y. R. Silberberg, R. Abeyaratne, R. D. Kamm, H. H. Asada, *Proc. Natl. Acad. Sci. U. S. A.* **2018**, *115*, E390.

[6] G. Burgstaller, B. Oehrle, M. Gerckens, E. S. White, H. B. Schiller, O. Eickelberg, *Eur. Respir. J.* **2017**, *50*, 1601805.

[7] J. Torgersen, X. H. Qin, Z. Li, A. Ovsianikov, R. Liska, J. Stampfl, *Adv. Funct. Mater.* **2013**, *23*, 4542.

**ADVANCED
SCIENCE NEWS**

www.advancedsciencenews.com

**ADVANCED
HEALTHCARE
MATERIALS**

www.advhealthmat.de

[8] K. Mandal, I. Wang, E. Vitiello, L. A. C. Orellana, M. Balland, *Nat. Commun.* **2014**, *5*, 5749.

[9] S. Engelhardt, E. Hoch, K. Borchers, W. Meyer, H. Krüger, G. E. M. Tovar, A. Gillner, *Biofabrication* **2011**, *3*, 025003.

[10] F. Guilak, D. M. Cohen, B. T. Estes, J. M. Gimble, W. Liedtke, C. S. Chen, *Cell Stem Cell* **2009**, *5*, 17.

[11] F. Zhang, M. W. King, *Adv. Healthcare Mater.* **2020**, *9*, 1901358.

[12] A. Shrestha, B. N. Allen, L. A. Wiley, B. A. Tucker, K. S. Worthington, *J. Ocul. Pharmacol. Ther.* **2019**, *36*, 42.

[13] D. Mandt, P. Gruber, M. Markovic, M. Tromayer, M. Rothbauer, S. R. Adam Kratz, S. F. Ali, J. Van Hoorick, W. Holnthoner, S. Mühleder, P. Dubruel, S. Van Vlierberghe, P. Ertl, R. Liska, A. Ovsianikov, *Int. J. Bioprint.* **2018**, *4*, 1.

[14] L. Knudsen, M. Ochs, *Histochem. Cell Biol.* **2018**, *150*, 661.

[15] W. Sun, B. Starly, A. C. Daly, J. A. Burdick, J. Groll, G. Skeldon, W. Shu, Y. Sakai, M. Shinohara, M. Nishikawa, J. Jang, D. W. Cho, M. Nie, S. Takeuchi, S. Ostrovidov, A. Khademhosseini, R. D. Kamm, V. Mironov, L. Moroni, I. T. Ozbolat, *Biofabrication* **2020**, *12*, 022002.

[16] R. Levato, T. Jungst, R. G. Scheuring, T. Blunk, J. Groll, J. Malda, *Adv. Mater.* **2020**, *32*, 1906423.

[17] J. Zhang, B. Hartmann, J. Siegel, G. Marchi, H. Clausen-Schaumann, S. Sudhop, H. P. Huber, *PLoS One* **2018**, *13*, e0195479.

[18] E. D'Arcangelo, A. P. McGuigan, *BioTechniques* **2015**, *58*, 13.

[19] K. A. Kilian, B. Bugarija, B. T. Lahn, M. Mrksich, *Proc. Natl. Acad. Sci. U. S. A.* **2010**, *107*, 4872.

[20] M. J. Dalby, N. Gadegaard, R. Tare, A. Andar, M. O. Riehle, P. Herzyk, C. D. W. Wilkinson, R. O. C. Oreffo, *Nat. Mater.* **2007**, *6*, 997.

[21] J. Van Hoorick, L. Tytgat, A. Dobos, H. Ottevaere, J. Van Erps, H. Thienpont, A. Ovsianikov, P. Dubruel, S. Van Vlierberghe, *Acta Biomater.* **2019**, *97*, 46.

[22] E. D. Lemma, B. Spagnolo, M. De Vittorio, F. Pisanello, *Trends Biotechnol.* **2019**, *37*, 358.

[23] P. N. Bernal, P. Delrot, D. Loterie, Y. Li, J. Malda, C. Moser, R. Levato, *Adv. Mater.* **2019**, *31*, 1904209.

[24] B. Grigoryan, S. J. Paulsen, D. C. Corbett, D. W. Sazer, C. L. Fortin, A. J. Zaita, P. T. Greenfield, N. J. Calafat, J. P. Gounley, A. H. Ta, F. Johansson, A. Randles, J. E. Rosenkrantz, J. D. Louis-Rosenberg, P. A. Galie, K. R. Stevens, J. S. Miller, *Science* **2019**, *364*, 458.

[25] T. Bückmann, N. Stenger, M. Kadic, J. Kaschke, A. Frölich, T. Kennerknecht, C. Eberl, M. Thiel, M. Wegener, *Adv. Mater.* **2012**, *24*, 2710.

[26] B. Richter, V. Hahn, S. Bertels, T. K. Claus, M. Wegener, G. Delaittre, C. Barner-Kowollik, M. Bastmeyer, **2017**, *29*, 1604342.

[27] N. Silbernagel, A. Körner, J. Balitzki, M. Jaggy, S. Bertels, B. Richter, M. Hippler, A. Hellwig, M. Hecker, M. Bastmeyer, N. D. Ullrich, *Biomaterials* **2020**, *227*, 119551.

[28] S. Basu, L. P. Cunningham, G. D. Pins, K. A. Bush, R. Taboada, A. R. Howell, J. Wang, P. J. Campagnola, *Biomacromolecules* **2005**, *6*, 1465.

[29] J. Ma, C. Li, N. Huang, X. Wang, M. Tong, A. H. W. Ngan, B. P. Chan, *ACS Appl. Mater. Interfaces* **2017**, *9*, 29469.

[30] B. P. Chan, J. N. Ma, J. Y. Xu, C. W. Li, J. P. Cheng, S. H. Cheng, *Adv. Funct. Mater.* **2014**, *24*, 277.

[31] P. J. Su, Q. A. Tran, J. J. Fong, K. W. Eliceiri, B. M. Ogle, P. J. Campagnola, *Biomacromolecules* **2012**, *13*, 2917.

[32] E. C. Spivey, E. T. Ritschdorff, J. L. Connell, C. A. McLennon, C. E. Schmidt, J. B. Shear, *Adv. Funct. Mater.* **2013**, *23*, 333.

[33] D. Serien, S. Takeuchi, *ACS Biomater. Sci. Eng.* **2017**, *3*, 487.

[34] A. Nishiguchi, G. Kapiti, J. R. Höhner, S. Singh, M. Moeller, *ACS Appl. Biol. Mater.* **2020**, *3*, 2378.

[35] K. Yue, G. Trujillo-de Santiago, M. M. Alvarez, A. Tamayol, N. Annabi, A. Khademhosseini, *Biomaterials* **2015**, *73*, 254.

[36] G. Ying, N. Jiang, C. Yu, Y. S. Zhang, *Bio-Des. Manuf.* **2018**, *1*, 215.

[37] L. Brigo, A. Urciuolo, S. Giulitti, G. Della Giustina, M. Tromayer, R. Liska, N. Elvassore, G. Brusatin, *Acta Biomater.* **2017**, *55*, 373.

[38] A. Ovsianikov, A. Deiwick, S. Van Vlierberghe, M. Pflaum, M. Wilhelmi, P. Dubruel, B. Chichkov, *Materials* **2010**, *4*, 288.

[39] F. A. Pennacchio, C. Fedele, S. De Martino, S. Cavalli, R. Vecchione, P. A. Netti, *ACS Appl. Mater. Interfaces* **2018**, *10*, 91.

[40] J. Van Hoorick, P. Gruber, M. Markovic, M. Tromayer, J. Van Erps, H. Thienpont, R. Liska, A. Ovsianikov, P. Dubruel, S. Van Vlierberghe, *Biomacromolecules* **2017**, *18*, 3260.

[41] G. Burgstaller, A. Sengupta, S. Vierkotten, G. Preissler, M. Lindner, J. Behr, M. Königshoff, O. Eickelberg, *Am. J. Physiol.: Lung Cell. Mol. Physiol.* **2018**, *314*, L708.

[42] M. Ihnatouski, J. Pauk, D. Karev, B. Karev, *Materials* **2020**, *13*, 2302.

[43] M. Zhu, Y. Wang, G. Ferracci, J. Zheng, N. J. Cho, B. H. Lee, *Sci. Rep.* **2019**, *9*, 6863.

[44] K. Cicha, T. Koch, J. Torgersen, Z. Li, R. Liska, J. Stampfl, *J. Appl. Phys.* **2012**, *112*, 094906.

[45] E. D. Lemma, F. Rizzi, T. Dattoma, B. Spagnolo, A. Sileo, A. Qualtieri, M. De Vittorio, F. Pisanello, *IEEE Trans. Nanotechnol.* **2017**, *16*, 23.

[46] C. L. Lay, Y. H. Lee, M. R. Lee, Y. Phang, X. Y. Ling, *ACS Appl. Mater. Interfaces* **2016**, *8*, 8145.

[47] C. Prein, N. Warmbold, Z. Farkas, M. Schieker, A. Aszodi, H. Clausen-Schaumann, *Matrix Biol.* **2016**, *50*, 1.

[48] S. Dex, P. Alberton, L. Willkomm, T. Söllradl, S. Bago, S. Milz, M. Shakibaei, A. Ignatius, W. Bloch, H. Clausen-Schaumann, C. Shukunami, M. Schieker, D. Docheva, *EBioMedicine* **2017**, *20*, 240.

[49] D. Muschter, L. Fleischhauer, S. Taheri, A. F. Schilling, H. Clausen-Schaumann, S. Grässel, *Bone* **2020**, *133*, 115181.

[50] R. Reuten, T. R. Patel, M. McDougall, N. Rama, D. Nikodemus, B. Gibert, J. G. Delcros, C. Prein, M. Meier, S. Metzger, Z. Zhou, J. Kaltenberg, K. K. McKee, T. Bald, T. Tüting, P. Zigrino, V. Djonov, W. Bloch, H. Clausen-Schaumann, E. Poschl, P. D. Yurchenco, M. Ehrbar, P. Mehlen, J. Stetefeld, M. Koch, *Nat. Commun.* **2016**, *7*, 13515.

[51] C. Y. Khripin, C. J. Brinker, B. Kaehr, *Soft Matter* **2010**, *6*, 2842. http://doi.org/10.1039/c001193b.

[52] F. A. Pennacchio, C. Casale, F. Urciuolo, G. Imparato, R. Vecchione, P. A. Netti, *Biomater. Sci.* **2018**, *6*, 2084.

[53] E. Hoch, T. Hirth, G. E. M. Tovar, K. Borchers, *J. Mater. Chem. B* **2013**, *1*, 5675.

[54] P. Cignoni, M. Callieri, M. Corsini, M. Dellepiane, F. Ganovelli, G. Ranzuglia, in *Sixth Eurographics Italian Chapter Conference*, (Eds: V. Scarano, R. De Chiara, U. Erra), Eurographics Association, Darmstadt, Germany **2008**, pp. 129–136.

[55] K. Parkatzidis, M. Chatzinikolaidou, M. Kaliva, A. Bakopoulou, M. Farsari, M. Vamvakaki, *ACS Biomater. Sci. Eng.* **2019**, *5*, 6161.

[56] R. Sodian, M. Loebe, A. Hein, D. P. Martin, S. P. Hoerstrup, E. V. Potapov, H. Hausmann, T. Lueth, R. Hetzer, *ASAIO J.* **2002**, *48*, 12.

[57] M. Leiss, K. Beckmann, A. Girós, M. Costell, R. Fässler, *Curr. Opin. Cell Biol.* **2008**, *20*, 502.

[58] C. Claaßen, M. H. Claaßen, V. Truffault, L. Sewald, G. E. M. Tovar, K. Borchers, A. Southan, *Biomacromolecules* **2018**, *19*, 42.

[59] L. Sewald, C. Claaßen, T. Götz, M. H. Claaßen, V. Truffault, G. E. M. Tovar, A. Southan, K. Borchers, *Macromol. Biosci.* **2018**, *18*, 1800168.

[60] P. Alberton, H. C. Dugonitsch, B. Hartmann, P. Li, Z. Farkas, M. M. Saller, H. Clausen-Schaumann, A. Aszodi, *Int. J. Mol. Sci.* **2019**, *20*, 1008.

[61] P. Li, L. Fleischhauer, C. Nicolae, C. Prein, Z. Farkas, M. M. Saller, W. C. Prall, R. Wagener, J. Heilig, A. Niehoff, H. Clausen-Schaumann, P. Alberton, A. Aszodi, *Int. J. Mol. Sci.* **2020**, *21*, 666.

[62] C. D. O'connell, B. Zhang, C. Onofrillo, S. Duchi, R. Blanchard, A. Quigley, J. Bourke, S. Gambhir, R. Kapsa, C. Di Bella, P. Choong, G. G. Wallace, *Soft Matter* **2018**, *14*, 2142.

[63] S. Xin, D. Chimene, J. E. Garza, A. K. Gaharwar, D. L. Alge, *Biomater. Sci.* **2019**, *7*, 1179.

[64] J. Roether, S. Bertels, C. Oelschlaeger, M. Bastmeyer, N. Willenbacher, *PLoS One* **2018**, *13*, e0207397.

2000918 (14 of 15)

**ADVANCED
SCIENCE NEWS**

www.advancedsciencenews.com

**ADVANCED
HEALTHCARE
MATERIALS**

www.advhealthmat.de

[65] K.-S. Lee, D.-Y. Yang, S. H. Park, T. W. Lim, R. H. Kim, *2006 Int. Symp. on Biophotonics, Nanophotonics Metamaterials, Hangzhou*, IEEE, Piscataway, NJ **2006**, pp. 8–14.

[66] J. Stampfl, R. Liska, A. Ovsianikov, *Multiphoton Lithography: Techniques, Materials, and Applications*, Wiley-VCH, Weinheim **2017**.

[67] H. Chen, J. Zhong, J. Wang, R. Huang, X. Qiao, H. Wang, Z. Tan, *Int. J. Nanomed.* **2019**, *14*, 937.

[68] P. Linke, R. Suzuki, A. Yamamoto, M. Nakahata, M. Kengaku, T. Fujiwara, T. Ohzono, M. Tanaka, *Langmuir* **2019**, *35*, 7538.

[69] M. Hörning, S. Kidoaki, T. Kawano, K. Yoshikawa, *Biophys. J.* **2012**, *102*, 379.

[70] M. Hörning, M. Nakahata, P. Linke, A. Yamamoto, M. Veschgini, S. Kaufmann, Y. Takashima, A. Harada, M. Tanaka, *Sci. Rep.* **2017**, *7*, 7660.

[71] T. Peng, K. Thorn, T. Schroeder, L. Wang, F. J. Theis, C. Marr, N. Navab, *Nat. Commun.* **2017**, *8*, 14836.

[72] S. Romanazzo, G. Forte, M. Ebara, K. Uto, S. Pagliari, T. Aoyagi, E. Traversa, A. Taniguchi, *Sci. Technol. Adv. Mater.* **2012**, *13*, 064211.

[73] J. Li, L. Zhang, L. Yu, I. Minami, S. Miyagawa, M. Hörning, J. Dong, J. Qiao, X. Qu, Y. Hua, Fujimoto, Y. Shiba, Y. Zhao, F. Tang, S. Miyagawa, Y. Chen, Y. Sawa, C. Tang, L. Liu, *Commun. Biol.* **2020**, *3*, 122.

[74] D. Yaffe, S. Ora, *Nature* **1977**, *270*, 725.

[75] S. M. Murphy, M. Kiely, P. M. Jakeman, P. A. Kiely, B. P. Carson, *Biosci. Rep.* **2016**, *36*, e00330.

[76] S. Zhao, M. I. Todorov, R. Cai, A.-M. Rami, H. Steinke, E. Kemter, H. Mai, Z. Rong, M. Warmer, M. Stanic, *Cell* **2020**, *180*, 796.

[77] G. Lovric, *Ph.D. Thesis*, Swiss Federal Institute of Technology, Zurich **2015**.

[78] M. Hippler, E. D. Lemma, S. Bertels, E. Blasco, C. Barner-Kowollik, M. Wegener, M. Bastmeyer, *Adv. Mater.* **2019**, *31*, 1808110.

[79] R. Prevedel, A. Diz-Muñoz, G. Ruocco, G. Antonacci, *Nat. Methods* **2019**, *16*, 969.

[80] V. Hahn, P. Kiefer, T. Frenzel, J. Qu, E. Blasco, C. Barner-Kowollik, M. Wegener, *Adv. Funct. Mater.* **2020**, *30*, 1907795.

[81] T. Niendorf, L. Frydman, M. Neeman, E. Seeliger, *Acta Physiol.* **2020**, *228*, e13392.

[82] H. Yin, M. D. Caceres, Z. Yan, M. Schieker, M. Nerlich, D. Docheva, *Biochem. Biophys. Res. Commun.* **2019**, *512*, 691.

[83] B. A. Pryce, A. E. Brent, N. D. Murchison, C. J. Tabin, R. Schweitzer, *Dev. Dyn.* **2007**, *236*, 1677.

[84] A. J. Garcia, M. D. Vega, D. Boettiger, *Mol. Biol. Cell* **1999**, *10*, 785.

[85] I. N. Sneddon, *Int. J. Eng. Sci.* **1965**, *3*, 47.

[86] D. Docheva, D. Padula, C. Popov, W. Mutschler, H. Clausen-Schaumann, M. Schieker, *J. Cell. Mol. Med.* **2008**, *12*, 537.

[87] R. Álvarez-Asencio, E. Thormann, M. W. Rutland, *Rev. Sci. Instrum.* **2013**, *84*, 096102.

[88] B. Hartmann, L. Fleischhauer, CANTER Processing Tool, https://github.com/CANTERhm/Canter_Matlab_Library (accessed: May **2020**).

[89] A. Zemel, F. Rehfeldt, A. E. X. Brown, D. E. Discher, S. A. Safran, *Nat. Phys.* **2010**, *6*, 468.

[90] S. Inoue, V. Frank, M. Hörning, S. Kaufmann, H. Y. Yoshikawa, J. P. Madsen, A. L. Lewis, S. P. Armes, M. Tanaka, *Biomater. Sci.* **2015**, *3*, 1539.

[91] N. Otsu, *IEEE Trans. Syst. Man. Cybern.* **1979**, *9*, 62, (accessed: May **2020**).

[92] Y.-L. Sun, Q. Li, S.-M. Sun, J.-C. Huang, B.-Y. Zheng, Q.-D. Chen, Z.-Z. Shao, H.-B. Sun, *Nat. Commun.* **2015**, *6*, 8612.

[93] M. Lunzer, L. Shi, O. G. Andriotis, P. Gruber, M. Markovic, P. J. Thurner, D. Ossipov, R. Liska, A. Ovsianikov, *Angew. Chem.* **2018**, *130*, 15342.

[94] M. H. Tong, N. Huang, W. Zhang, Z. L. Zhou, A. H. W. Ngan, Y. Du, B. P. Chan, *Sci. Rep.* **2016**, *6*, 1.

[95] P. Kiefer, V. Hahn, M. Nardi, L. Yang, E. Blasco, B.-K. Christopher, M. Wegener, *Advanced Optical Materials* **2020**, 2000895. http://doi.org/10.1002/adom.202000895.

[96] C. Bock, M. Boutros, J. G. Camp, L. Clarke, H. Clevers, J. A. Knoblich, P. Liberali, A. Regev, A. C. Rios, O. Stegle, H. G. Stunnenberg, S. A. Teichmann, B. Treutlein, R. G. J. Vries, the Human Cell Atlas 'Biological Network' Organoids, *zenodo* **2020**, https://zenodo.org/badge/DOI/10.5281/zenodo.4001718.svg.